Chapter 6
Observation of Sea Surface Wind and Wave in X-Band TerraSAR-X and TanDEM-X Over Hurricane Sandy

XiaoMing Li and Susanne Lehner

Abstract Several TerraSAR-X and TanDEM-X ScanSAR images are acquired in October, 2012 to track the Hurricane Sandy. Three of the images are acquired in the open sea, which are presented in this chapter to demonstrate observations of sea surface wind and wave extracted from X-band ScanSAR image with high spatial resolution of 17 m in the hurricane. In the case of the TerraSAR-X image acquired on October 26, 2012, we analyze the peak wave direction and length of swell generated by Hurricane Sandy, as well as interaction of swell with the Abaco Island, Bahamas. In the other two cases, sea surface wind field derived from the TerraSAR-X and TanDEM-X acquired on October 27 and 28 are presented. The sea surface wind speed retrieved by the X-band Geophysical Model Function (GMF) XMOD2 using wind direction derived from SAR images and the NOAA Hurricane Research Division (HRD) wind analyses are both presented for comparisons. We also compare the retrieved sea surface wind speed with Stepped Frequency Microwave Radiometer (SFMR) to quantify effect of rainfall on X-band SAR images.

6.1 Introduction

Tropical cyclones (TCs) are storm systems characterized by a large low pressure center that normally produce strong winds and heavy rainfall, as well as able to produce high waves and damaging storm surge when the TCs make their landfall over coastal regions. Thanks to spaceborne observations, TCs can be frequently

X. Li (✉)
Institute of Remote Sensing and Digital Earth, Chinese Academy of Sciences, Beijing, People's Republic of China
e-mail: lixm@radi.ac.cn

X. Li
Hainan Key Laboratory of Earth Observation, Sanya, People's Republic of China

S. Lehner
Remote Sensing Technology Institute, German Aerospace Center (DLR), Oberpfaffenhofen, Germany
e-mail: Susanne.Lehner@dlr.de

X. Li (ed.), *Hurricane Monitoring With Spaceborne Synthetic Aperture Radar*, Springer Natural Hazards, DOI 10.1007/978-981-10-2893-9_6

observed from space for analysis of wind, wave, rainfall, temperature and cloud-top properties. The qualitative and quantitative information of TC derived from satellite observations have been recognized as a crucial for improving numerical predictions of TC in short term and hindcast for climatology studies, e.g., as demonstrated by Velden et al. [1] for hurricane tracking forecast and by Zhang et al. [2] for Pacific typhoon reanalysis.

The spaceborne active remote sensing have the unique capability of observing sea surface through cloud, which has been playing an important role of monitoring response of sea surface under extreme weather situations. Scatterometers on board the European Remote Sensing (ERS), the Quick Scatterometer (QuikSCAT), and the Meteorological Operational (MetOp) satellites are particularly suitable for measurements of sea surface wind field, as both wind direction and wind speed can be derived without needing external information. Another active remote sensing instrument, spaceborne Synthetic Aperture Radar (SAR), e.g., the ERS-1/2 SAR, ENVISAT/ASAR, RADARSAT-1/2, TS-X/TD-X and Cosmo-Skymed, can not only provide sea surface backscatter intensity like scatterometer, but also image the sea surface in two-dimension with large spatial coverage and high spatial resolution, which provides abundant oceanic and atmospheric information of TCs, such as hurricane-generated long swell waves in small scales [3, 4], hurricane/typhoon eye morphology [5] and roll vortices occurred in marine boundary layer [6] in meso-scale.

With respect to measurements of sea surface wind field in TCs using scatterometer or SAR, two major sources may limit the accuracy of retrieval for high winds: (1) deficiencies of the Geophysical Model Function (GMF) for high winds, as presented in [7]. Improvement of GMF, such as CMOD5 [8] is dedicated for retrieval of high wind using scatterometer or SAR data, has somewhat reduces this error sources for inversion of sea surface wind field in hurricane scale [9]. However, one still faces the problem of speed ambiguity when applying CMOD5 for retrieving high winds [10] and saturation or damping of radar signal under severe weather conditions [11]. (2) Effects of heavy rains on radar signal. Microwave signals are likely to suffer effect of heavy rains which are permanent features in TCs and therefore errors are induced of deriving sea surface wind speed, e.g., studies presented by Quilfen et al. [7] and Weissman et al. [12]. Yueh et al. [13] proposed an updated GMF for retrieval of sea surface wind field considering the rain rate as a parameter, which is applied to the hurricane Floyd with maximum wind speed reaching 60 m/s showing a good agreement NOAA Hurricane Research Division (HRD) wind reanalysis.

The new generation spaceborne SAR sensors, such as represented by RADARSAT-2, TerraSAR-X/TanDEM-X (TS-X/TD-X) and Cosmo-Skymed, are highlighted by their high spatial resolution (down to 1 m), flexible imaging modes and polarimetric capabilities. Some preliminary studies related to TCs are presented for sea surface wind field retrieval for Typhoon Megi [14] using TS-X data and Hurricane Earl [15] using RASARSAT-2 data. In this chapter, we present detailed analysis of sea surface wind and wave field derived from three TS-X and TD-X images acquired over Hurricane Sandy.

6.2 TerraSAR-X and Tandem-X Data

The German X-band SAR TS-X was launched successfully on 15 June 2007 from Baikonur, Kazakhstan. The satellite is in a near-polar orbit around the Earth, at an altitude of 514 km. Using its active radar antenna, TS-X is able to produce image data with a resolution down to one meter, independent of weather conditions and daylight. It has been fully operational since January 7, 2008. Main technical parameters of TS-X are briefed in Table 6.1. The detailed information of TS-X mission, design, as well as ground segment is available in [16, 17]. Figure 6.1 illuminates three different imaging modes of TS-X, i.e., Spotlight, Stripmap and ScanSAR modes. For both Stripmap and ScanSAR modes, the radar beam can be electronically tilted within a range of 20–45° perpendicular to the flight direction without having to move the satellite itself. For Spotlight mode, the radar beam can be further tilted to 55°. Scenes sizes and resolutions of the three imaging modes of TS-X are listed in Table 6.2.

Table 6.1 Main TerraSAR-X system parameters

Height	4.88 m
Width	2.4 m
Payload mass	About 400 kg
Radar frequency	9.65 GHz
Power consumption	800 watt (on average)
Resolution	1, 3 m, or 16 m depending on image size
Polarization	HH/VV/HV/VH
Orbit altitude	514 km
Inclination	97.4°, sun-synchronous
Mission life time	At least 5 years

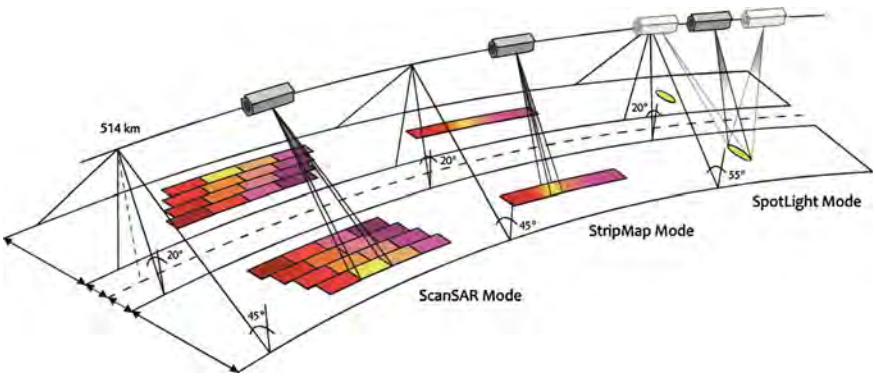

Fig. 6.1 Illumination of TS-X imaging modes (© DLR)

Table 6.2 Features of TS-X imaging modes

Imaging mode	Resolution (Range × Azimuth)	Scene size (Range × Azimuth)
Spotlight	1 m × 1.5 m . . . 3.5 m	10 km × 5 km (variable)
cStripmap	3 m × 3 m	30 km × 50 km (variable)
ScanSAR	16 m × 16 m	100 km × 150 km (variable)

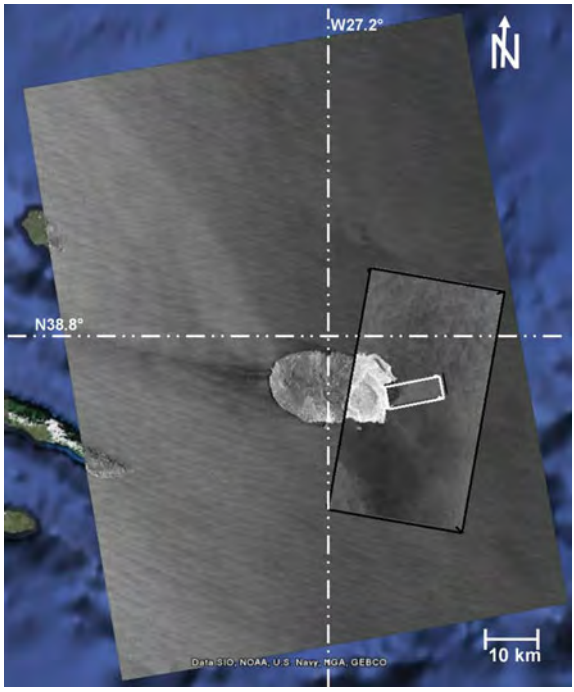

Fig. 6.2 Overlay of TSX ScanSAR (largest one) image acquired on March 20, 2008, StripMap image (in the *black rectangle*) acquired on January 15, 2009 and Spotlight mode image (in the *white rectangle*) acquired on March 26, 2008 over Terceira island (map in background © Google earth)

To demonstrate variable applications of TS-X in different imaging modes in oceanography, three quick looks of TS-X images over the Terceira Island in the North Atlantic operated respectively in ScanSAR, StripMap and Spotlight mode overlaid on top of each other are shown in Fig. 6.2 [18]. The ScanSAR image has the largest area coverage of 140 and 100 km in azimuth and range direction, respectively, with a pixel size of 8.25 m.

Wind streaks are visible in the ScanSAR image, and surface wind blowing toward northwest is inferred by the shadow zone behind the Santa Barbara volcano (1021 m) at the NW end of the island. The ScanSAR image yields an overview of sea state and wind field for the entire oceanic region around the island. The StripMap image (inside the black rectangle) acquired in the eastern coast of Terceira island shows spatial variations of wave refraction when approaching to the coasts. The Spotlight image inside the white rectangle has the smallest coverage of 5 km in azimuth and

12 km in range, which is are particularly suitable for investigation of near-shore processes, harbor monitoring, and targets detection.

The TanDEM-X (TerraSAR-X add-on for Digital Elevation Measurement, TD-X) mission was launched successfully as well on June 21, 2010. The first bistatic SAR mission is formed by adding a second while almost identical X-band SAR to TS-X, which opens a new era in spaceborne radar remote sensing. The twins can operate either collaboratively, e.g., in bistatic and monostatic modes, or independently.

6.3 X-Band GMF for Sea Surface Wind Retrieval from TS-X and TD-X

The X-band Geophysical Model Function (GMF) called XMOD2 [5] is used for retrieval of the sea surface wind field from TS-X and TD-X. Brief description of XMOD2 is given in following.

XMOD2 is written as

$$z(v, \phi, \theta) = B_0^p(v, \theta)(1 + B_1(v, \theta)cos\phi + B_2(v, \theta)cos2\phi) \tag{6.1}$$

where B_0, B_1, and B_2 are functions of incidence angle θ and sea surface wind speed v at 10 m height. Relative direction ϕ is the angle between wind direction ϕ and radar look direction α, i.e. $\phi = \varphi - \alpha$. The constant p has value of 0.625. In the proposed GMF XMOD2 for X-band SAR, transfer functions used to depict B_0 and B_2 are adopted from the CMOD5, while a second-order polynomial function is used to describe the dependence of B_1 on the sea surface wind speed and incidence angle as given in Eq. (6.2).

$$B_1 = \sum_{j=0}^{2} \sum_{i=0}^{2} \alpha_{ij} \theta^i v^i \tag{6.2}$$

In total, 32 coefficients are included in XMOD2, which are determined by tuning dataset consisting of in situ buoy measurements (371 collocations) and DWD (German Weather Service) analysis atmospheric model (639 collocations). Figure 6.3 shows the simulated for X-band TS-X using the XMOD2 for incidence angles of 20°, 30° and 40° against the relative sea surface wind direction.

The simulation shows that the XMOD2 can represent properly the anisotropic effect of wind direction on the sea surface backscatter. Moreover, the incidence angle effect on the difference between upwind and crosswind, as well as on the difference between upwind and downwind, are also distinct. One can find that the higher incidence angle, the more sensitive is on the sea surface wind direction. Figure 6.4a and b show the simulated sea surface backscatter using XMOD2 for incidence angles of 20°, 30° and 40° in upwind and cross wind situations. The same simulations but using the CMOD5 are also presented for comparison. It is interesting

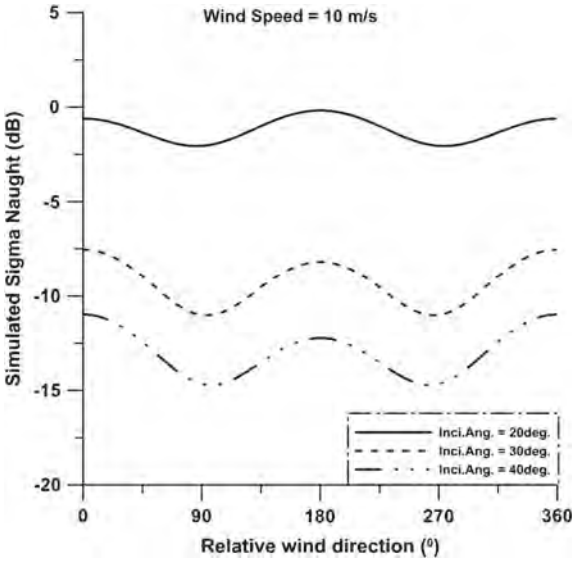

Fig. 6.3 Simulated sea surface backscatter in X-band SAR using the XMOD2 for incidence angles of 20°, 30°, and 40° against the relative sea surface wind direction in the sea surface wind speed of 10 m/s

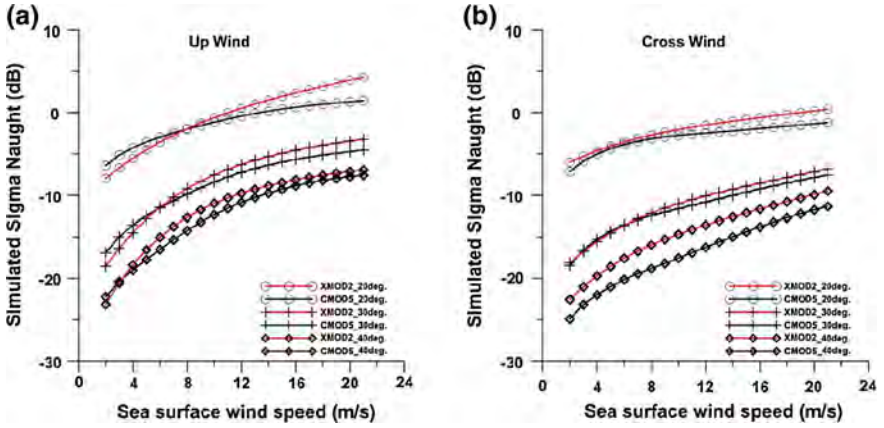

Fig. 6.4 Simulated σ_0 in X-band SAR using the XMOD2 for incidence angles of 20°, 30°, and 40° against the sea surface wind speed in upwind (**a**) and crosswind (**b**), as represented by *black lines*. The *red lines* show the simulation of σ_0 in C-band SAR using the CMOD5 for comparison

to notice that, for upwind, the transition of the difference between X-band and C-band σ_0 shows a dependence on incidence angle. For incidence of 20°, 30°, and 40°, the transition appears at around 8, 6 and 4 m/s.

In order to reduce irregular distributions of wind speed and wind direction in the tuning dataset, large amount of DWD wind model results, which is around two

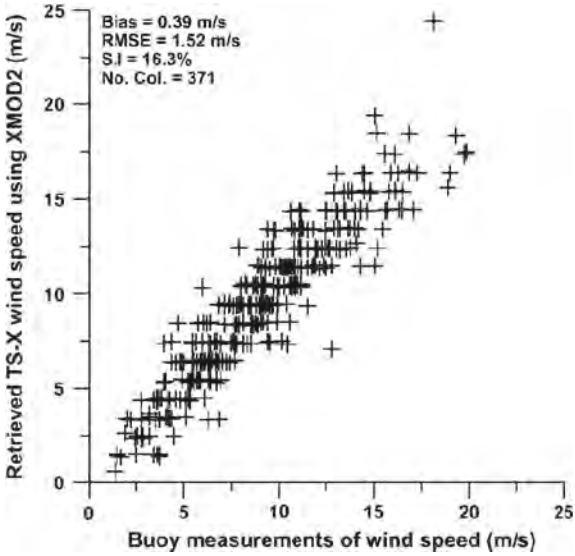

Fig. 6.5 Comparison of the retrieved TS-X/TD-X U_{10} using the XMOD2 against in situ buoy measurements. Buoy measurements of the sea surface wind direction is used as input for the retrieval

times of the collocated buoy amount, is also added in the tuning dataset. Therefore, comparison of the retrieved sea surface wind speeds to buoy measurements is still necessary to verify XMOD2. The collocated buoy measurements of wind direction, incidence angle and averaged sea surface backscatter σ_0 of the TS-X subscenes are used as input to XMOD2 to retrieve the sea surface wind speed. The comparison is shown in Fig. 6.5.

6.4 Analysis of TS-X and TD-X Data for Hurricane Sandy

When the two X-band SAR sensors operate independently, it can increase opportunity to track oceanic or atmospheric phenomena with significant temporal and spatial variations, such as tropical cyclones analyzed in this chapter. The three colorful rectangles shown in Fig. 6.6 represent three ScanSAR images acquired by TS-X or TD-X in VV polarizations on October 26, 27, and 28, respectively. Acquisition details of the three X-band ScanSAR images over the Hurricane Sandy are given in Table 6.3.

6.4.1 Observation on October, 26

Two continuous TS-X ScanSAR scenes are acquired in descending orbit on October, 26 at 11:17 UTC, as indicated by the two pink rectangles in Fig. 6.6. The first scene

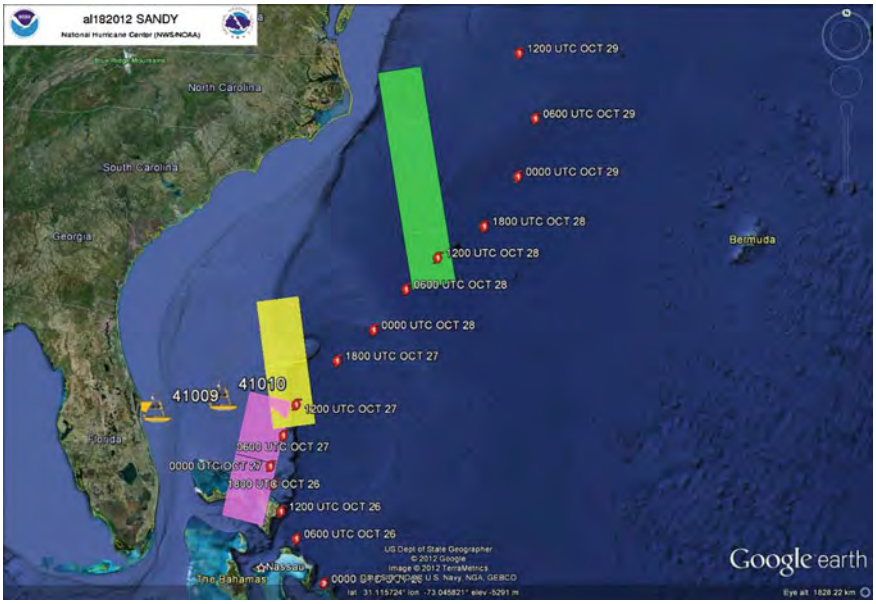

Fig. 6.6 TS-X and TD-X acquisitions over the Hurricane Sandy. The *pink*, *yellow* and *green rectangles* represent the X-band ScanSAR images on October 26, 27, and 28, respectively. Best track of the Hurricane Sandy issued by NOAA is overplayed on the Google Earth map

Table 6.3 Acquisitions of TS-X and TD-X ScanSAR images over the Hurricane Sandy

Mission	Time	Incidence angle	Distance to Hurricane center
TS-X	2012-10-26T 11:17 UTC	19.6° – 30.3°	~36 km
TS-X	2012-10-27T 23:05 UTC	33.9° – 42.3°	~170 km
TD-X	2012-10-28T 22:50 UTC	31.7° – 40.5°	~190 km

acquired in open sea, about 70 km away to the north of the Abaco island, Bahamas, is shown in right panel of Fig. 6.7.

The key to derive surface wave information, e.g., peak wavelength and direction, directly from SAR image spectra without through nonlinear inversion [19] is that SAR should image linearly the sea surface waves under certain conditions. The velocity-bunching mechanism [20] plays an important role on whether surface waves are imaged linearly or not by SAR. To quantify whether SAR images surface waves in linear or nonlinear regime, a critical velocity-bunching cutoff significant wave height (H_s) given in [21] is represented here.

$$H_s = \frac{1}{\pi^{3/2}\sqrt{g}} \frac{v}{h} \frac{\lambda^{3/2}}{\sqrt{1 + tan^2\theta sin^2\phi cos\phi}} \tag{6.3}$$

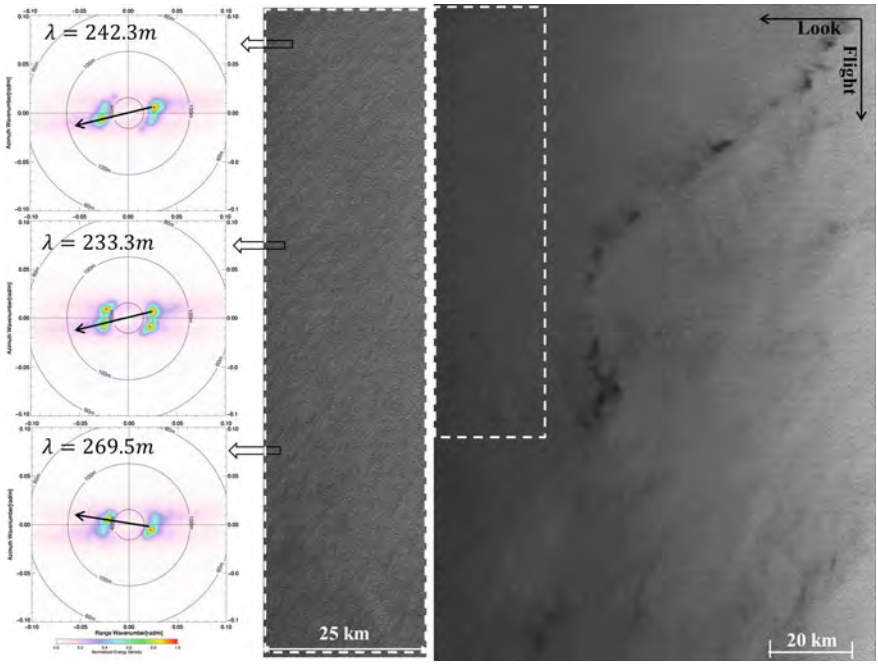

Fig. 6.7 The TS-X ScanSAR first scene (*right panel*) acquired on October 26, 2012 at 11:17 UTC near to Hurricane Sandy. The *right panel* shows the sub-image in the *white rectangle* and image spectra

where v is satellite velocity and h is satellite orbit altitude. For TS-X and TD-X, v has a value of 7.6 km/s which is similar with the previous spaceborne SAR sensors such as ERS/SAR, RADARSAT and ENVISAT/ASAR. However, orbit altitude of TS-X and TD-X is 514 km, which is much lower than those platforms. λ is cutoff wavelength in unit of meter. θ is incidence angle in degree. The relative angle between surface wave propagation and flight (azimuth) direction is defined as ϕ. For azimuth traveling waves, $\phi = 0°$ and for range traveling waves, $\phi = 90°$. Prior to deriving wave parameters directly from TS-X image spectra, we firstly analyze whether sea state conditions are favorable for TS-X imaging sea surface linearly.

In this case, the NOAA/NDBC buoy 41010 locates around 60 km west of the TS-X first scene, as indicated in Fig. 6.6. The buoy measurements at 11:20 UTC on October 26, 2012 are listed in Table 6.4. As the mean wave direction is not available in buoy 41010, we further add measurements of buoy 41009 for analysis, which is 220 km away from the TS-X image.

The dispersion relation of surface waves in finite depth water is:

$$\omega^2 = gktan(kH) \tag{6.4}$$

Table 6.4 TS-X Collocated Buoy 41010 and 41009 measurements

Buoy ID	Time	Hs	Dominant Peak period	Mean wave direction	Wind speed	Water depth
41010	11:20 UTC	7.18 m	12.12 s	N/A	18.7 m/s	872.6 m
41009	11:50 UTC	5.79 m	12.12 s	83°	15.1 m/s	40.5 m

where ω is wave frequency, k is wave number and H is water depth, respectively. By knowing the measured dominant peak period T, the calculated peak wavelength in location of buoy 41010 and 41009 is 229.5 and 196.5 m, respectively. Although buoy 41009 is about 160 km away from buoy 41010, we notice that the dominant peak periods measured by both buoys are identical.

Buoy 41010 locates near to far range of the TS-X image, where incidence angle is 30.3°. Therefore, estimated velocity-bunching cutoff significant wave height using Eq. (6.3) against wave propagation direction between 0° and 80° for incidence angle of θ 30° and cutoff wavelength λ is plotted in Fig. 6.8. Although mean wave direction is not available in buoy 41010, we can infer that it should be near to 83° from measurements of buoy 41009. Azimuth angle of the TS-X image is 190.8° clockwise relative to North. Therefore, angle ϕ in Eq. (6.3), i.e. wave propagation relative to SAR azimuth is 72.2°. Figure 6.8 indicates that the cutoff H_s for ϕ = 72° and 73° is 6.8 and 7.2 m, respectively, which is near to H_s of 7.18 m measured by buoy 41010. Therefore, it is inferred that the TS-X under this condition can image swell waves linearly, which ensures that we can use SAR image spectra derived from TS-X to analyze swell wave propagation in this case.

Three image spectra derived from sub-image are shown in left panel of Fig. 6.7. The image spectra are derived from subscene with pixel size of 1024 x 1024, which

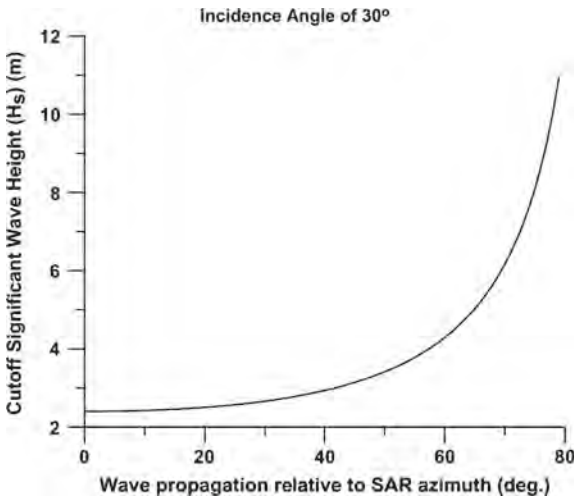

Fig. 6.8 Estimated cutoff H_s of TS-X as a function of wave propagation direction relative to SAR azimuth for incidence angle of 30° and cutoff wavelength of 250 m

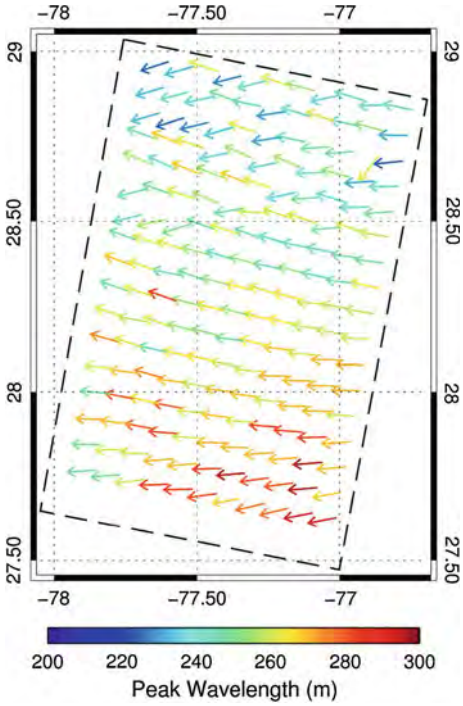

Fig. 6.9 Peak wavelength and direction from SAR image spectra for the TS-X scene shown in *right panel* of Fig. 6.7

corresponds to a spatial size of 8.5 km × 8.5 km. Each subscene is further divided into four small subsets with pixel size of 256 × 256 (around 2 km × 2 km). Then the four corresponding FFT spectra are summed and averaged as the image spectrum for a subscene. The second image spectra shows peak wavelength is 233.3 m which agrees well with buoy 41010 measurement of 229.5 m. The peak wave direction has a slight change of around 20° from north to south within the sub-image. Figure 6.9 shows the peak wavelength and direction from SAR image spectra for the whole TS-X scene to demonstrate spatial variations of swell generated by Hurricane Sandy. 180° ambiguity of wave propagation direction derived from SAR image spectrum is removed based on buoy measurement. Over the image sea surface, swell wavelength is longer than 220 m. The peak wavelength increases homogeneously from around 220 to 300 m from northwest to southeast. Over the sea above 28.5°N, the peak wave direction varies between northeast and east. It should indicate a crossing swell sea state, as also observed in the second image spectra shown in Fig. 6.7. However, the southern water region shows that swell comes homogeneously from east with peak wavelength near to 300 m.

The second TS-X scene acquired on October 26 is shown in Fig. 6.10. It covers the northern and southern coastal region of the Abaco island. Land in the lower right part of the image is the Great Abaco and the Little Abaco is in the middle of the image. On “top” of Great and Little Abaco, there is a long chain of islands consist

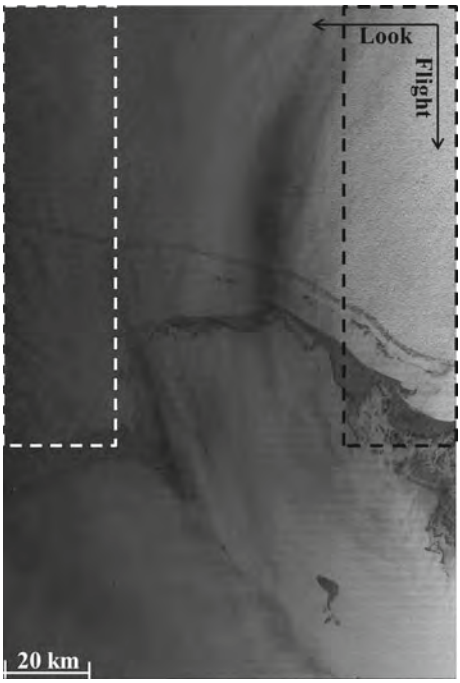

Fig. 6.10 The second TS-X scene acquired on October 26, 2012 at 11:17 UTC over the Abaco islands, Bahamas

of a large amount of sand bank and coral reefs in shallow water, which block the hurricane generated waves propagating further to south. Therefore, in the second TS-X scenes, we can clearly observe that sea state exhibits significant spatial variations in the northern and southern water regions of the long chain of islands.

Figure 6.11 shows the two sub-images inside the rectangles shown in Fig. 6.10. Two SAR image spectra are derived from subscenes in the two areas are shown as well. The two image spectra derived from the sub-image in right panel shows consistent peak wavelength and direction with those derived in the first TS-X scene shown in Fig. 6.9. The long island chain in the north of the Abaco island plays a role as a barrier which blocks swell further propagates toward to the island coast. In the left panel, the first SAR image spectrum is derived from subscene in the north of the island chain, which also shows consistent swell peak wavelength and direction with those in the near range sub-image (right panel). However, in the second SAR image spectrum which is derived from subscene locates in the south of the island chain, we observe a peak locates in the inner circle in order of kilometers, which is much longer than wavelength of swell observed in the north. It is inferred as the peak of wind streaks. Wind direction is perpendicular to connected line of the inner peaks, as indicated by dash line in the image spectrum. The other peak, however, only has wavelength of 209 m, which is 105 m shorter than swell wavelength in the north of the island chain. Further, we also notice that peak wave direction (solid line) of this wave system is close to wind direction. Thus, it should be the young swell

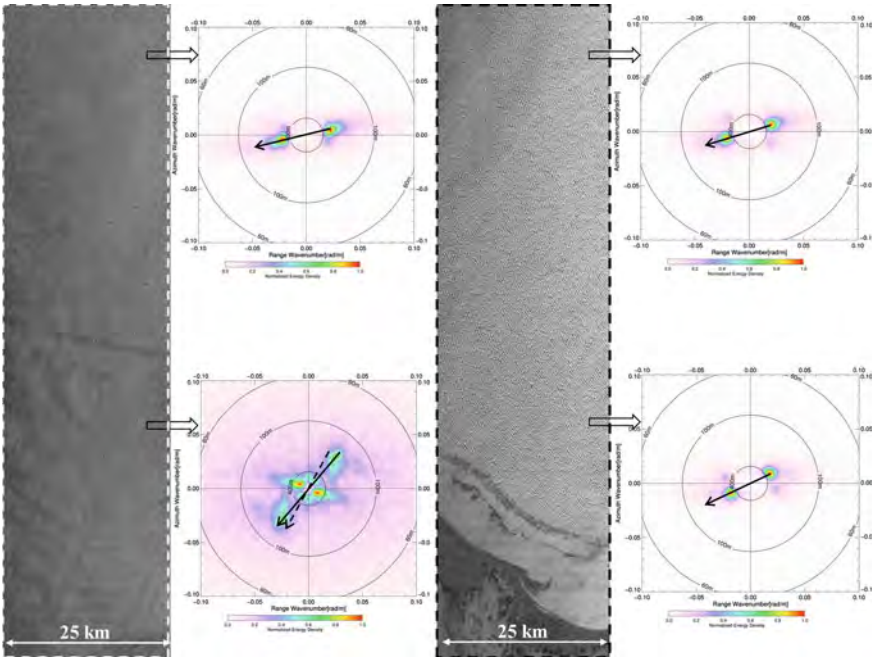

Fig. 6.11 Sub-images in the near (*right panel*) and far (*left panel*) range of the TS-X image and SAR image spectra. *Solid lines* indicate wave direction. *Dash line* indicates wind direction

generated by local hurricane wind, as most incoming long swells are blocked by the island chain. Therefore, this special situation provides us an opportunity for further investigation of wave growth in hurricane scale wind field.

6.4.2 Observations on October, 27 and 28

TS-X and TD-X acquired another two images over Hurricane Sandy on October 27 and 28, respectively, as represented by the yellow and green rectangles in Fig. 6.6. With respect to the two images, we focus on sea surface wind field analysis, particularly to verify performance of the XMOD2 for sea surface wind retrieval in extreme weather situations.

6.4.2.1 TS-X/TD-X Images and Retrieved Sea Surface Wind Field

Figure 6.12a and b show the HRD sea surface wind field on October 27 and 28 at 22:30 UTC, respectively. Spatial coverage of the TS-X images represented by white rectangles is overlaid on the HRD wind field map. The black lines show track

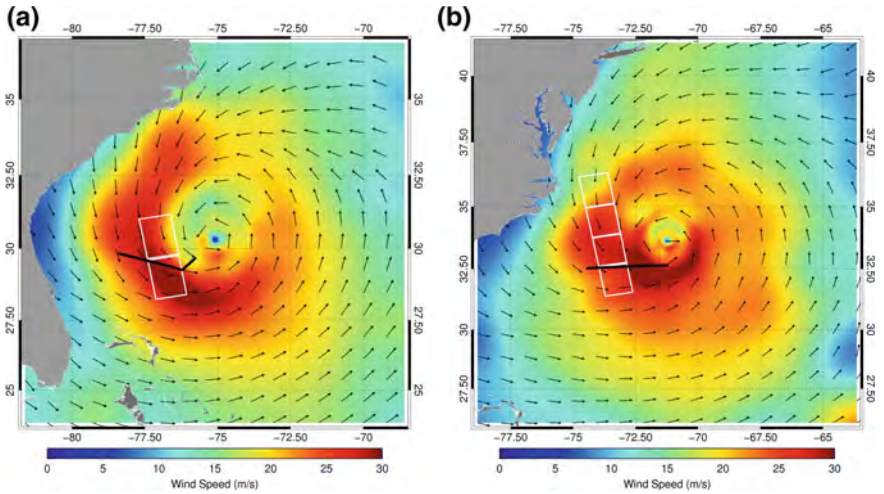

Fig. 6.12 HRD sea surface wind field at **a** on October 27 and October 28 **b** at 22:30 UTC. *White rectangles* represent spatial coverage of the TS-X image acquired at 23:05 UTC on October 27 and 22:50 UTC on October 28. *Block line* shows the track of aircraft within 30 min of SAR acquisitions

of the US aircraft which obtained the Stepped Frequency Microwave Radiometer (SFMR) measurements at close time (within 30 min) to SAR acquisitions. The TS-X calibrated image on October 27 at 23:05 UTC and October 28 at 22:50 UTC is shown in Figs. 6.13a and 6.14a, respectively. In both cases, we dont observe complete eye structure in the SAR images. However, from characters of the image, e.g., large contrast of sea surface backscatter, we may refer that both are acquired near to center of Sandy, which on the other hand indicates that Sandy has a big size considering that swath width of the TS-X/TD-X ScanSAR is 100 km.

As SAR has only one antenna, sea surface wind direction has to be obtained firstly in order to retrieve sea surface wind speed from SAR image by exploiting GMFs. In both cases, wind direction obtained from HRD analysis wind field are used a priori to retrieve the sea surface wind speed by XMOD2. The results are shown in Figs. 6.13b and 6.14b, respectively. The other way to obtain sea surface wind direction is to use FFT method (e.g., [22]) or Local Gradient (LG) method [23] if wind streaks are visible in SAR images. Figures 6.13c and 6.14c are the retrieved sea surface wind speed using wind direction derived from SAR images through the FFT method for the TS-X and TD-X cases, respectively. The HRD wind direction generally agrees well with that derived from SAR images directly. With respect to the case on October 27, we find that the major differences between HRD and TS-X wind directions are in lower left part of the image, i.e. the southwest quadrant. The HRD wind direction has a bias of around 15° compared to wind streaks visible in the TS-X image, which in turn induces the retrieved wind speed around 5 m/s lower than that by using wind direction derived from wind streaks in the TS-X image. We also observe that the sea

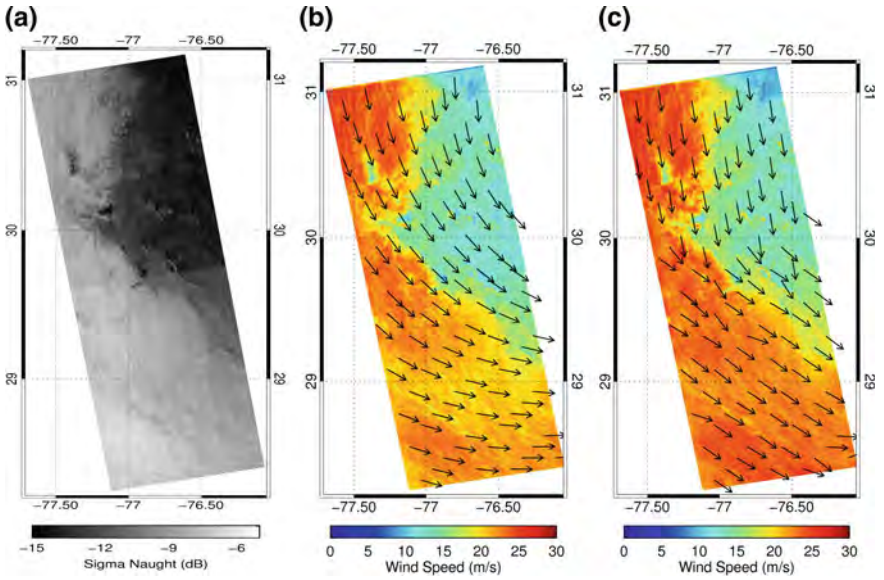

Fig. 6.13 **a** TS-X calibrated image acquired on October 27 at 23:05 UTC. **b** Retrieved TS-X wind speed using HRD wind direction; **c** Retrieved TS-X wind speed using TS-X wind direction

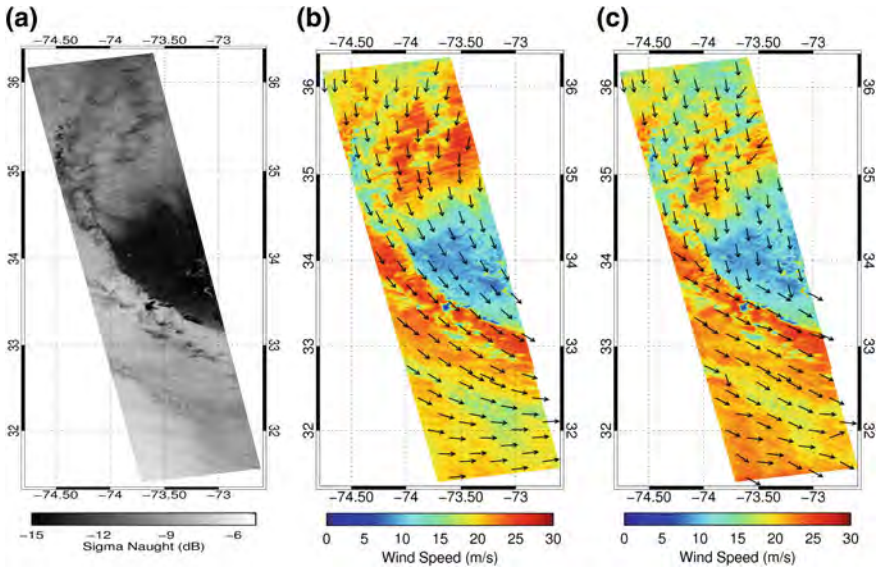

Fig. 6.14 **a** TS-X calibrated image acquired on October 28 at 22:50 UTC. **b** Retrieved TS-X wind speed using HRD wind direction; **c** Retrieved TS-X wind speed using TS-X wind direction

surface wind speed retrieved by using TD-X wind direction is higher than that by using the HRD wind direction in the southwest quadrant in the second case.

6.4.2.2 Influence of Rainfall on X-Band SAR Data and Its Retrieved Sea Surface Wind Field

On both TS-X and TD-X images, we can observe effect of rainfall on X-band SAR data, for instance, one can find some bright slicks in the large dark pattern area in both images. The rain band of Sandy is also clearly visible in the TD-X image (Fig. 6.14 (a)). In a previous study, Melsheimer et al. [24] investigate effects of rain cell on SAR imagery using SIRC/X-SAR data in multifrequency (L-, C-, and X-band) and multipolarization (HH, VV and HV). They summarized that the radar backscatter over ocean in the presence of rain cells is mainly associated with three processes: (1) scattering and attenuation of radar microwaves by hydrometeors in atmosphere, (2) the modification (enhancement or reduction) of sea surface roughness by rain drops, and 3) the enhanced sea surface roughness by wind gust. Generally, the latter two processes are easily identified in SAR imagery as both can significantly change the sea surface roughness. However, if the radar microwaves are attenuated by rain cell in atmosphere, it maybe not as clearly manifested in SAR image as other processes, particularly when rain fall has a large spatial coverage such as in hurricanes or typhoons. To quantify attenuation of radar backscatter induced by rain fall, Urlaby [25] proposed a radiative transfer model for C-band radar. Danklmayer and Chandra [26] present a model to quantify the attenuation for Ka- and X- band SAR. This two-way path attenuation model is given as:

$$A(t) = r(t) \cdot 2 \cdot \frac{H}{cos\theta}\,[dB] \tag{6.5}$$

where, H is rain layer height, θ is local incidence angle of SAR. $r(t)$ is the attenuation coefficient in unit of dB/km, which is calculated via rain rate:

$$r(t) = a \cdot R^b \tag{6.6}$$

in which, R is rain rate in unit of mm/hr. The regression coefficients a and b is 0.0136 and 1.15 for X-band microwave. We use this model and rain rate measured by SFRM to quantify attenuation of X-band SAR radar backscatter induced by rain fall in Hurricane Sandy.

Figure 6.15a and b show the retrieved SAR sea surface wind speed (red line) and collocated SFMR measurements of sea surface wind speed (blue line) and rain rate (black line) on October 27 and October 28, respectively. The retrieved SAR sea surface wind speed shows a trend of underestimation compared to SFMR measurements, which tends to be consistent with rainfall rate measured as well by the SFMR.

We calculate X-band radar backscatter using the SFMR measurements of the sea surface wind speed, wind direction and incidence angle derived from SAR, which

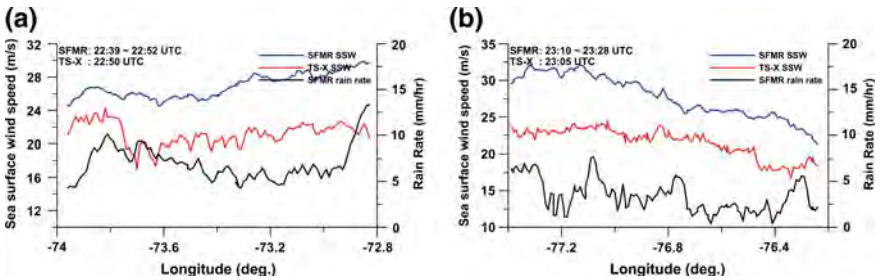

Fig. 6.15 Comparisons of SAR retrieved sea surface wind speed and SFMR measurements on October 27 (**a**) and October 28 (**b**)

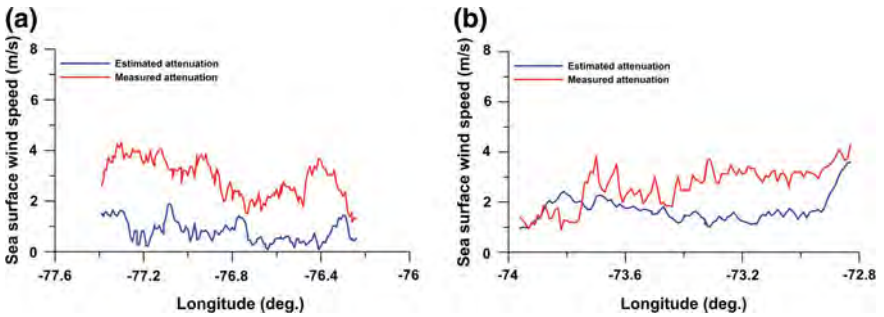

Fig. 6.16 Comparisons of estimated X-band SAR attenuation induced by rain fall to measured attenuation on October 27 (**a**) and October 28 (**b**)

is denoted σ_0^{sim}. It is assumed that the differences between observed TS-X/TD-X radar backscatter σ_0^{SAR} and the simulation σ_0^{sim} is the attenuation $\Delta\sigma$ induced by rain fall. By applying SFMR measurements of rain fall rate to Eqs. (6.5) and (6.6), the X-band SAR attenuation $\Delta\widetilde{\sigma}$ is estimated. Figure 6.16a and b shows the comparisons between $\Delta\sigma$ and $\Delta\widetilde{\sigma}$ for the TS-X and TD-X case, respectively. However, as shown in Fig. 6.15a and b, the estimated attenuation $\Delta\widetilde{\sigma}$ (blue line) is still lower than the calculated $\Delta\sigma$ (red line) with mean value of 2 dB and 1 dB for the case on October 27 and October 28, respectively. This indicates that attenuation of radar backscatter induced by rain fall in X-band SAR should be stronger than that estimated by Eq. (6.5). Comparing Figs. 6.15 with 6.14, we can find that if rain fall rate is larger than 5 mm/hr, e.g., in the case on October 28, the estimated attenuation $\Delta\widetilde{\sigma}$ by Eq. (6.5) shows better agreement with $\Delta\sigma$ than that in the case on October 27 which has rain rate lower than 5 mm/hr. Nevertheless, we need further investigation to investigate rain fall attenuation on X-band SAR data more accurately.

6.5 Discussion and Conclusion

Three X-band TS-X and TD-X ScanSAR images with swath width of 100 km and spatial resolution of 17 m acquired over Hurricane Sandy are presented. For the TS-X image acquired on October 26, 2012 over the Abaco island, we focus on analyzing spatial variations of hurricane generated swell. In order to derive peak wave parameters directly from the SAR image spectra, the so-called cutoff H_s is calculated using buoy measurements. Although sea state of this case is very rough with H_s of 7.18 m, the calculated cutoff H_s indicates that imaging of sea surface waves by TS-X under this situation is still a linear process. This should attribute to the orbit altitude of TS-X and TD-X (514 km) is much lower than that of the conventional spaceborne SAR sensors, such as RADARSAT and ENVISAT/ASAR (790 km). The TS-X image spectra in this case show that the long island chain of the Abaco island blocks swell propagates further towards to coastal area. Therefore, only windsea and young swell waves are observed behind the island, which are generated purely by local hurricane wind.

The sea surface wind fields are derived from the TS-X and TD-X images acquired on October 27 and 28, respectively by using XMOD2. To retrieve sea surface wind speed from SAR by applying GMF, the sea surface wind direction has to be obtained firstly. In both cases, the HRD wind direction is used for sea surface wind speed retrieval from TS-X and TD-X data. However, we found that HRD wind direction has a bias of around 15° compared with wind direction derived from SAR wind streaks in the southwest quadrant, which in turn induces a bias of around 5 m/s for the retrieved wind speed. This finding indicates that wind direction derived from SAR images may improvement the analysis wind field in TCs. The comparisons of the SAR retrieved wind speed with SFMR measurements show a negative bias of 6.2 and 5.8 m/s. It is noticed that the underestimation of SAR wind speed tends to be related with rainfall rate measured by SFMR as well. Although we try to simulate the attenuation induced by rain fall in X-band SAR using rain rate measured by SFMR, it is found that the simulated attenuation is still much lower than that estimated using TS-X/TD-X and SFMR measurements. The interesting finding is that the simulated attenuation shows better agreement with estimated one in the case on October 28 with rain rate above 5 mm/hr than that in the case on October 27 with rain rate lower than 5 mm/hr. Therefore, we consider that on the one hand XMOD2 needs to be further improvement, particularly for high winds. On the other hand, X-band SAR tends be rather sensitive to rain fall even for rain rate lower than 5 mm/hr. Thus, we also need improved model or method to relate rain rate with attenuation of radar backscatter in X-band SAR.

References

1. Velden, C.S., C.M. Hayden, W.P. Menzel, J.L. Franklin, and J.S. Lynch. 1992. The impact of satellite-derived winds on numerical hurricane track forecasting, weather and forecast. *Weather and Forecast* 7 (1): 107–118.
2. Zhang, X., T. Li, F. Weng, C.C. Wu, and L. Xu. 2007. Reanalysis of western Pacific typhoons in 2004 with multi-satellite observations. *Meteorology and Atmospheric Physics* 97 (1): 3–18.
3. Holt, B., A.K. Liu, D.W. Wang, A. Gnanadesikan, and H.S. Chen. 1998. Tracking storm-generated waves in the Northeast Pacific Ocean with ERS-1 synthetic aperture radar imagery and buoys. *Journal of Geophysical Research* 103 (C4): 7917–7929.
4. Li, X., W.G. Pichel, M. He, S. Wu, K.S. Friedman, P. Clemente-Colon, and C. Zhao. 2002. Observation of hurricane-generated ocean swell refraction at the Gulf Stream North Wall with the RADARSAT-1 synthetic aperture radar. *IEEE Transactions on Geoscience and Remote Sensing* 40 (10): 2131–2142.
5. Li, X.M., and S. Lehner. 2014. Algorithm for sea surface wind retrieval from TerraSAR-X and TanDEM-X data. *IEEE Transactions on Geoscience and Remote Sensing* 52 (5): 2928–2939.
6. Katsaros, K.B., P.W. Vachon, P.G. Black, P.P. Dodge, and E.W. Uhlhorn. 2000. Wind fields from SAR: Could they improve our understanding of storm dynamics? *Johns Hopkings APL Technical Digest* 21 (1): 86–93.
7. Quilfen, Y., B. Chapron, T. Elfouhaily, K. Katsaros, and J. Tournadre. 2003. Observation of tropical cyclones by high-resolution scatterometry. *Journal of Geophysical Research: Oceans* 103 (C4): 7767–7786.
8. Hersbach, H., A. Stoffelen, and S. de Haan. 2007. An improved C-band scatterometer ocean geophysical model function: CMOD5. *Journal of Geophysical Research: Oceans* 112 (C3).
9. Horstmann, J., D.R. Thompson, F. Monaldo, S. Iris, and H.C. Graber. 2005. Can synthetic aperture radars be used to estimate hurricane force winds? *Geophysical Research Letters* 32 (22).
10. Shen, H., W. Perrie, and Y. He. 2006. A new hurricane wind retrieval algorithm for SAR images. *Geophysical Research Letters* 33 (21).
11. Reppucci, A., S. Lehner, J. Schulz-Stellenfleth, and S. Brusch. 2010. Tropical cyclone intensity estimated from wide-swath SAR images. *IEEE Transactions on Geoscience and Remote Sensing* 48 (4): 1639–1649.
12. Weissman, D.E., M.A. Bourassa, and J. Tongue. 2002. Effects of rain rate and wind magnitude on Sea Winds scatterometer wind speed errors. *Weather and Forecast* 19 (5): 738–746.
13. Yueh, S.H., B.W. Stiles, W.Y. Tsai, H. Hu, and W.T. Liu. 2001. QuikSCAT geophysical model function for tropical cyclones and applications to Hurricane Floyd. *Meteorology and Atmospheric Physics* 39 (12): 2601–2612.
14. Li, X.M., and S. Lehner. 2001. Observation of typhoon Megi using TerraSAR-X data. Oberpfaffenhofen, Germany. TerraSAR-X Science Team Meeting.
15. Zhang, B., and W. Perrie. 2011. Cross-polarized synthetic aperture radar: A new potential measurement technique for hurricanes. *Bulletin of the American Meteorological Society* 93 (4): 531–541.
16. Werninghaus, R., and S. Buckreuss. 2010. The TerraSAR-X mission and system design. *IEEE Transactions on Geoscience and Remote Sensing* 48 (2): 606–614.
17. Bruckreuss, S., and B. Schttlerh. 2010. The TerraSAR-X ground segment. *IEEE Transactions on Geoscience and Remote Sensing* 48 (2): 623–631.
18. Li, X.M., S. Lehner, and W. Rosenthal. 2010. Investigation of ocean surface wave refraction using TerraSAR-X data. *IEEE Transactions on Geoscience and Remote Sensing* 48 (2): 830–840.
19. Hasselmann, K., and S. Hasselmann. 1991. On the nonlinear mapping of an ocean wave spectrum into a synthetic aperture radar image spectrum and its inversion. *Journal of Geophysical Research: Oceans* 96 (C6): 10713–10729.
20. Alpers, W.R., and C.L. Rufenach. 1979. The effect of orbital motions on synthetic aperture radar imagery of ocean waves. *IEEE Transactions on Antennas and Propagation* 27 (5): 685–690.

21. Raney, R.K., P.W. Vachon, R.A.D. Abreu, and A.S. Bhogal. 1989. Airborne SAR observations of ocean surface waves penetrating floating ice. *IEEE Transactions on Geoscience and Remote Sensing* 27 (5): 492–499.
22. Lehner, S., J. Horstmann, W. Koch, and W. Rosenthal. 1998. Mesoscale wind measurements using recalibrated ERS SAR image. *Journal of Geophysical Research: Oceans* 103 (C4): 7847–7856.
23. Koch, W. 2004. Directional analysis of SAR images aiming at wind direction. *IEEE Transactions on Geoscience and Remote Sensing* 42 (4): 702–710.
24. Melsheimer, C., W. Alpers, and M. Gade. 1998. Investigation of multifrequency/multipolarization radar signatures of rain cells over the ocean using SIR-C/X-SAR data. *Journal of Geophysical Research: Oceans* 103 (C9): 18867–18884.
25. Ulaby, F.T., R.K. More, and A.K. Fung. 1981. *Microwave remote sensing: Active and passive*. Massachusetts: Addison-Wesley.
26. Danklmayer, A., and M. Chandra. 2010. Precipitation Effects for X- and Ka-band SAR. Aachen, Germany. 8th European Conference on Synthetic Aperture Radar (EUSAR).